Zinc Pyrovanadate Nanoplates Embedded in Graphene Networks with Enhanced Electrochemical Performance

Yang Yu,[†,#] Chaojiang Niu,[†,#] Chunhua Han,*[,†] Kangning Zhao,[†] Jiashen Meng,[†] Xiaoming Xu,[†] Pengfei Zhang,[†,‡] Lei Wang,[†] Yuzhu Wu,[†] and Liqiang Mai*[,†]

[†]State Key Laboratory of Advanced Technology for Materials Synthesis and Processing, Wuhan University of Technology, Wuhan 430070, Hubei, China

[‡]Department of Chemistry, Shanghai Key Laboratory of Molecular Catalysis and Innovative Materials, Laboratory of Advanced Materials, Fudan University, Shanghai, 200433, China

S Supporting Information

ABSTRACT: Transition metal vanadates have gradually captured reseachers' attention as anode materials for lithium ion batteries, because of their high specific capacity and relatively high chemical stability. However, they suffer from low rate performance and short cycling performance because of the intrinsic low electronic conductivity and large volume variation during lithiation and delithiation. Here we report a design of zinc pyrovanadate nanoplates embedded in graphene networks through a facile one-pot hydrothermal method. Benefiting from graphene and zinc pyrovanadate nanoplates, this nanocomposite possesses high specific capacity, excellent rate capability, and superior cycling stability. Particularly, it exhibits a high reversible capacity of 902 mA h g^{-1} at 500 mA g^{-1}, maintaining 854 mA h g^{-1} after 400 cycles. The impressive electrochemical performance makes it a promising anode material for lithium ion batteries.
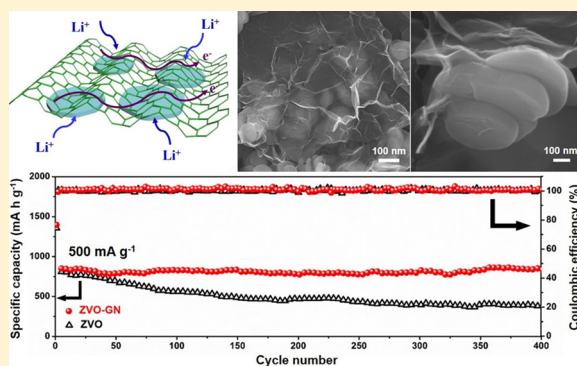
INTRODUCTION

Nowadays, the ever-increasing energy demand for novel, sustainable, and environmentally friendly energy sources has been a vital and challenging issue.[1−3] Among various available energy storage technologies, rechargeable lithium ion batteries (LIBs) with high capacity, long lifespan, no memory effect, and environmental benignity have been extensively applied in high-end consumer electronic devices.[4−8] However, conventional commercial graphite with relatively low theoretical capacity (372 mA h g^{-1}) may not be able to meet the tremendous demands of high-energy applications such as electric vehicles, plug-in hybrid electric vehicles, and further large-scale grid storage. Therefore, it is vital to seek new materials with high specific capacity, excellent rate capability, and long cycle life.[9,10]

Metal oxides, such as M$_x$O$_y$ (M = Co, Ni, Fe, V, Sn, etc.) have been considered as promising electrodes for the development of LIBs because of their high specific/volumetric capacity, high chemical stability, and low cost.[11−17] Besides simple binary metal oxides, ternary transition metal oxides, especially transition metal vanadates with abundant sources and relatively high ionic conductivity, have attracted many researchers' interests in electrochemical energy storage in recent years.[18−26] For example, Yang et al. reported Co$_3$V$_2$O$_8$ multilayered nanosheets as anode with enhanced cycling stability and rate capability and further investigated their electrochemical mechanisms. It was demonstrated that the reversible conversion reactions between CoO and Co

proceeded on the lithiated amorphous Li$_x$V$_2$O$_5$ matrices.[27] Sim et al. fabricated amorphous FeVO$_4$ nanosheet arrays directly grown on a flexible stainless steel substrate by a facile template-free and catalyst-free chemical vapor deposition (CVD) method, showing superior Li storage properties, especially at high current densities.[28] Zhao et al. presented graphene oxide wrapped amorphous copper vanadium oxides as LIB anodes with high-rate and long-life performance. Such excellent electrochemical properties result from the amorphous nature, dominant capacitive behavior, and enhanced electronic conductivity attributed to the in situ extraction of copper.[29] Besides, many vanadates contain crystal water, such as Co$_3$V$_2$O$_8$·nH$_2$O, FeVO$_4$·1.1H$_2$O, Cu$_3$V$_2$O$_7$(OH)$_2$·2H$_2$O, Zn$_3$V$_2$O$_7$(OH)$_2$·2H$_2$O, and so on. The crystal water, which exists as OH groups on the external and internal surfaces, enhances the reversible capacity, because the extra oxygen in the crystal water facilitates the formation of "Li−O" type binding in the low voltage reduction process.[30−32] However, the demand over good cycling performance for transition metal vanadates is still challenging.[33−36]

Graphene has been proven as an effective conducting support to host transition metal oxides in rechargeable batteries
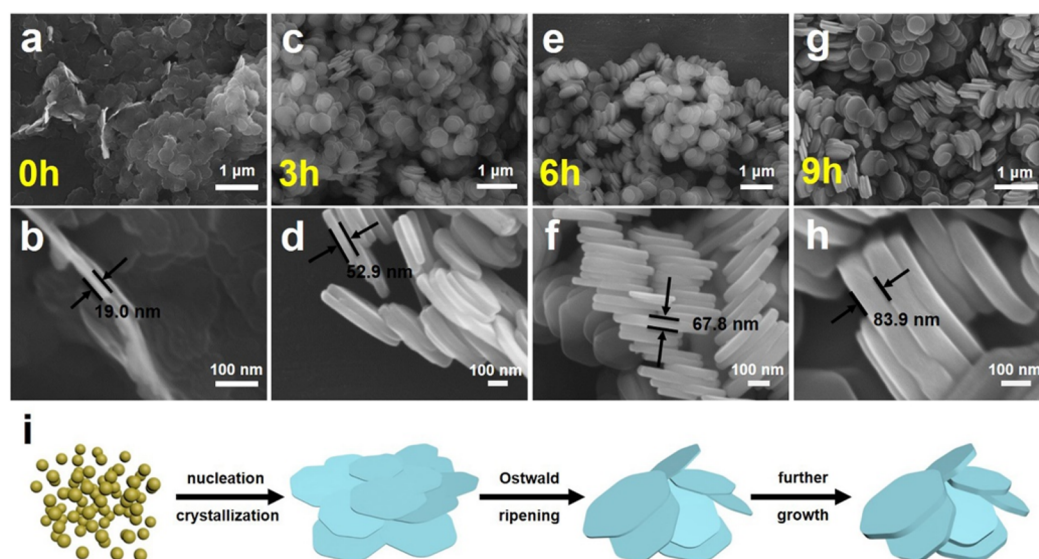
Figure 1. SEM images of the zinc pyrovanadate nanoplates prepared in (a,b) 0 h, (c,d) 3 h, (e,f) 6 h, and (g,h) 9 h. (i) Schematic of formation process of zinc pyrovanadate nanoplates.

because of its high electric conductivity, excellent mechanical flexibility, large specific surface area, and high chemical stability.[37−40] In addition, graphene could also act as an elastic buffer, accommodating the volume change during repeated lithium ion insertion/extraction, simultaneously preventing the agglomeration of nanoparticles and the cracking or crumbling of the electrode materials.[41−50] Therefore, realizing the combination of graphene and electrode materials is of great potential and significance.

Herein, we develop a facile one-pot hydrothermal route to synthesize the zinc pyrovanadate nanoplates embedded in graphene networks. To our knowledge, the formation mechanism, electrochemical performance, and lithium storage mechanism of this nanocomposite have been rarely reported before. This nanoarchitecture possesses both high structural integrity and excellent electronic conductivity, exhibiting great potential as anode for LIBs.

■ EXPERIMENTAL SECTION

Materials Preparation. Graphene oxide (GO) dispersion was prepared via a modified Hummer's method.[51] In a typical synthesis, 0.18 g of V_2O_5, 2.0 g of cetyltrimethylammonium bromide (CTAB), 2.5 g of NaOH, and 5 mL of as-prepared GO dispersion were orderly added into 25 mL of deionized water. After stirring for 10 min, 0.89 g of $Zn(NO_3)_2 \cdot 6H_2O$ was added into the above solution; a brown and viscous solution was rapidly formed. The solution was then transferred into a 50 mL Teflon-lined autoclave and maintained at 200 °C for 18 h. After the solution was cooled to room temperature, gray precipitate was collected and washed several times with deionized water and absolute ethanol and dried at 70 °C in air to get the zinc pyrovanadate nanoplates embedded in graphene networks (denoted as ZVO-GN). For comparison, pristine zinc pyrovanadate (denoted as ZVO) nanoplates were prepared using the similar procedure without adding GO dispersion.

Material Characterization. X-ray diffraction (XRD) data were collected with a Bruker D8 Discover X-ray diffractometer, using Cu Kα radiation (λ = 1.5418 Å) in a 2θ range from 10° to 80° at room temperature. Field emission scanning electron

microscopy (FESEM) images were collected using a JEOL-7100F scanning electron microscope. In addition, transmission electron microscopy (TEM) images associated with selected area electron diffraction (SAED) were collected using a JEM-2100F microscope, and energy dispersive X-ray spectra (EDS) were recorded using an Oxford IE250 system. Carbon content analysis was determined by Vario EL cube CHNSO elemental analyzer. Brunauer−Emmett−Teller (BET) surface areas were measured at 77 K using a Tristar II 3020 instrument. X-ray photoelectron spectroscopy (XPS) measurements and ther-mogravimetric-differential scanning calorimetry (TG-DSC) analyses were conducted using a VG MultiLab 2000 instrument and an STA-449C, respectively.

Electrochemical Measurement. The electrochemical properties were evaluated by assembling 2016 coin cells in a glovebox filled with pure argon gas. The working electrode was prepared by mixing the as-synthesized materials, acetylene black and carboxyl methyl cellulose (CMC) in a weight ratio of 70:25:5. The slurry was spread onto copper foil and dried in a vacuum oven at 70 °C for 24 h. The loading of the active materials was 1.3−1.8 mg cm^{-2}. Lithium chips were used as the counter electrode and reference electrode. The electrolyte was composed of 1 M $LiPF_6$ dissolved in ethylene carbonate (EC)-dimethyl carbonate (DMC) with a volume ratio of 1:1. Cyclic voltammetry (CV) test was performed using an electrochemical workstation (CHI 760S) in the voltage range of 0.01−3 V. Galvanostatic charge/discharge measurements were performed using a multichannel battery testing system (LAND CT2001A), and electrochemical impedance spectroscopy (EIS) was carried out with an Autolab Potentiostat Galvanostat. All of the measurements were carried out at room temperature.

■ RESULTS AND DISCUSSION

V_2O_5, NaOH, and CTAB are dissolved in deionized water as the precursor. The connection between V and O in solution is related to the pH value. When the pH value is adjusted to 9−13, condensation of the protonated HVO_4^{2-} occurs via oxolation, releasing the pyrovanadate ions ($V_2O_7^{4-}$).[52] Then $V_2O_7^{4-}$ coprecipitates with Zn^{2+} to form $Zn_3V_2O_7(OH)_2 \cdot 2H_2O$
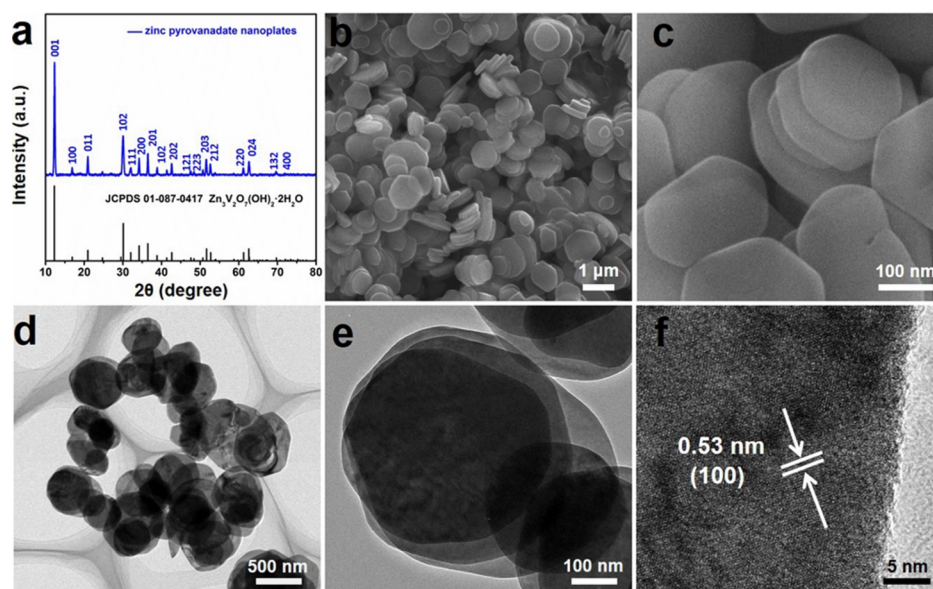
Figure 2. (a) XRD pattern, (b, c) SEM images (d,e) TEM images and (f) HRTEM image of zinc pyrovanadate nanoplates.
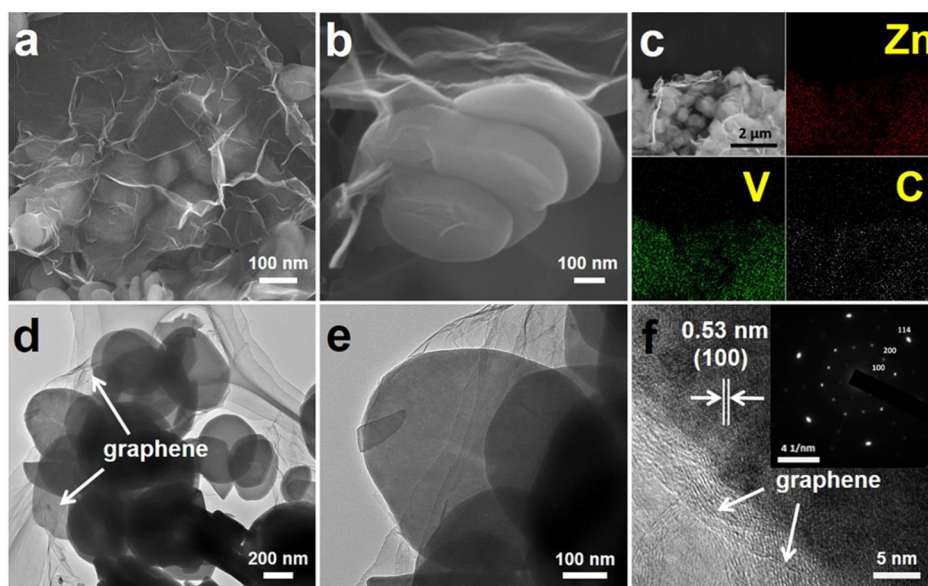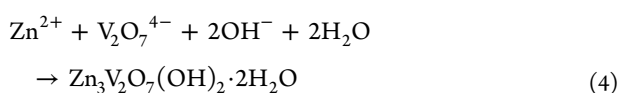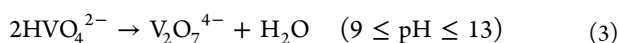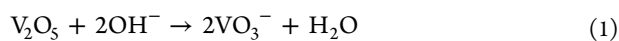

Figure 3. (a,b) SEM images, (c) EDS, (d,e) TEM images, (f) HRTEM image of zinc pyrovanadate nanoplates embedded in graphene networks, respectively. The inset of panel f shows the corresponding SAED pattern.

with the assistance of hydrothermal conditions. This process can be shown with the following equations:

$$V_2O_5 + 2OH^- \rightarrow 2VO_3^- + H_2O \qquad (1)$$

$$VO_3^- + OH^- \rightarrow HVO_4^{2-} \qquad (2)$$

$$2HVO_4^{2-} \rightarrow V_2O_7^{4-} + H_2O \quad (9 \leq pH \leq 13) \qquad (3)$$

$$Zn^{2+} + V_2O_7^{4-} + 2OH^- + 2H_2O$$
$$\rightarrow Zn_3V_2O_7(OH)_2 \cdot 2H_2O \qquad (4)$$

A time-dependent experiment is performed to explore and further understand the formation process of ZVO nanoplates (Figure 1). It is revealed that a large amount of irregular and thin nanosheets (∼20 nm) emerge in the initial stage without heating (Figure 1a,b). Some regular polygonal nanoplates

(thickness, ∼50 nm) appear after reacting for 3 h (Figure 1c,d). As Figure 1 panels e and f show, a reaction of 6 h results in thicker nanoplates (∼70 nm). When the reaction time is extended to 9 h, the thickness of each ZVO nanoplate increases to over 80 nm (Figure 1g,h). To sum up, with the reaction time extending, each ZVO nanoplate becomes thicker and its diameter remains in the range of 400−500 nm. In addition, the polygonal nanoplates tend to be round, and the oriented attachment of the nanoplates can be observed.

The XRD pattern (Figure 2a) of the ZVO nanoplates can be indexed to the hexagonal $Zn_3V_2O_7(OH)_2 \cdot 2H_2O$ phase (JCPDS 01-087-0417) with lattice parameters of $a = b = 6.0498$ Å, $c = 7.1960$ Å, and $\alpha = \beta = 90°$, $\gamma = 120°$, consistent with the space group $P\bar{3}m1$. In the structure of $Zn_3V_2O_7(OH)_2 \cdot 2H_2O$, the sandwich-like brucite type of layer is formed by close-packed terminal O atoms of pyrovanadate and hydroxide groups (Supporting Information, Figure S1). The Zn atoms occupy
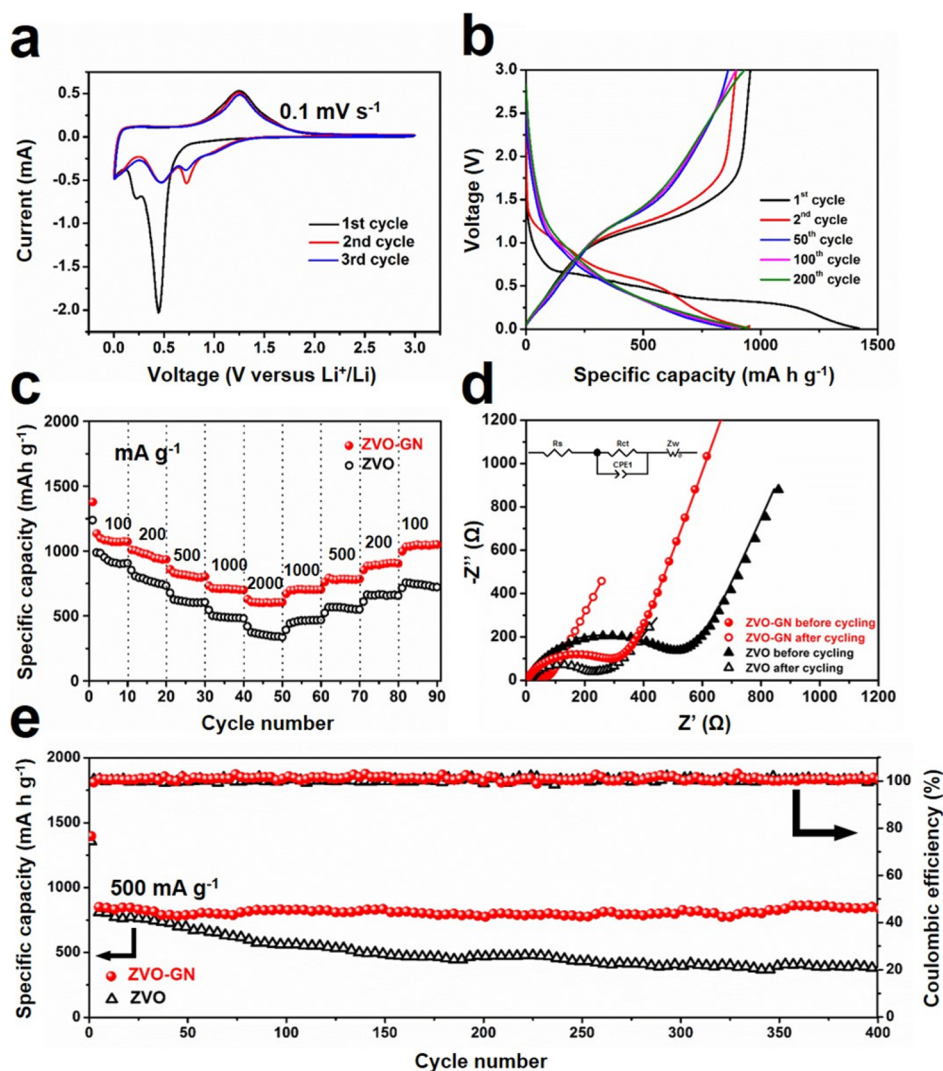
Figure 4. (a) CV curves of the zinc pyrovanadate nanoplates embedded in graphene networks obtained at a voltage range of 0.01 to 3.0 V (vs Li$^+$/Li) at a scan rate of 0.1 mV s^{-1}. (b) Galvanostatic charge and discharge curves of the 1st, 2nd, 50th, 100th, 200th cycles of the zinc pyrovanadate nanoplates embedded in graphene networks at a current density of 200 mA g^{-1}. (c) Rate performance of zinc pyrovanadate nanoplates and zinc pyrovanadate nanoplates embedded in graphene networks tested at rates of 100, 200, 500, 1000, and 2000 mA g^{-1}, (d) EIS of zinc pyrovanadate nanoplates and zinc pyrovanadate nanoplates embedded in graphene networks before and after cycling in the frequency range of 100 kHz to 0.01 Hz, respectively. The inset shows the equivalent circuit. (e) Cycling performance and Coulombic efficiency of zinc pyrovanadate nanoplates and zinc pyrovanadate nanoplates embedded in graphene networks measured at a current density of 500 mA g^{-1}, respectively.

three-quarters of the octahedral sites (purple, Figure S1). The remaining site is surrounded by V−O−V pillars (V$_2$O$_7^{4-}$ group, gray, Figure S1). And the OH$^-$ groups form hydrogen bonds to the water molecules that fill cavities in the porous framework.[53,54] The products display polygonal even round plate-like morphologies and uniform distribution (Figure 2b,d). Each nanoplate has a planar size in the range of 400−500 nm and its thickness is ∼100 nm. (Figure 2c,e). The HRTEM image (Figure 2f) shows the typical Zn$_3$V$_2$O$_7$(OH)$_2$·2H$_2$O lattice fringes of the as-synthesized ZVO. The measured interplanar spacing is 0.53 nm, which corresponds to that of (100) planes of hexagonal Zn$_3$V$_2$O$_7$(OH)$_2$·2H$_2$O.

To increase the conductivity and structural integrity of ZVO nanoplates, graphene oxide (GO) is introduced into the synthesis. Because of the strong intensities of the diffraction peaks from well-crystallized ZVO obtained at 200 °C for 18 h and the small quantity of graphene, no obvious characteristic peaks of graphene are observed in the XRD pattern of ZVO-

GN (Figure S2). The ZVO nanoplates are homogeneously embedded in ultrathin graphene networks (Figure 3a,d). EDS results show that the zinc, vanadium, and carbon are distributed uniformly in the final product (Figure 3c). The graphene shows a typical wrinkled morphology, and the ZVO nanoplates are overlapped and surrounded by graphene nanosheets (Figure 3b,e). The HRTEM image (Figure 3f) shows the typical Zn$_3$V$_2$O$_7$(OH)$_2$·2H$_2$O lattice fringes and the surrounding ultrathin graphene nanosheets of ZVO-GN. Similar to ZVO nanoplates, the measured interplanar spacing is 0.53 nm, corresponding to (100) planes of hexagonal Zn$_3$V$_2$O$_7$(OH)$_2$·2H$_2$O. The SAED image (the inset of Figure 3f) reveals the single crystalline nature of Zn$_3$V$_2$O$_7$(OH)$_2$·2H$_2$O.

Raman spectra (Figure S3a) indicate the existence of Zn$_3$V$_2$O$_7$(OH)$_2$·2H$_2$O and graphene in the composite. The bands in the ranges of 270−550 cm^{-1} and 640−1050 cm^{-1} represent the Zn$_3$V$_2$O$_7$(OH)$_2$·2H$_2$O bands, and the bands in the ranges of 1200−1450 cm^{-1} and 1510−1650 cm^{-1} are
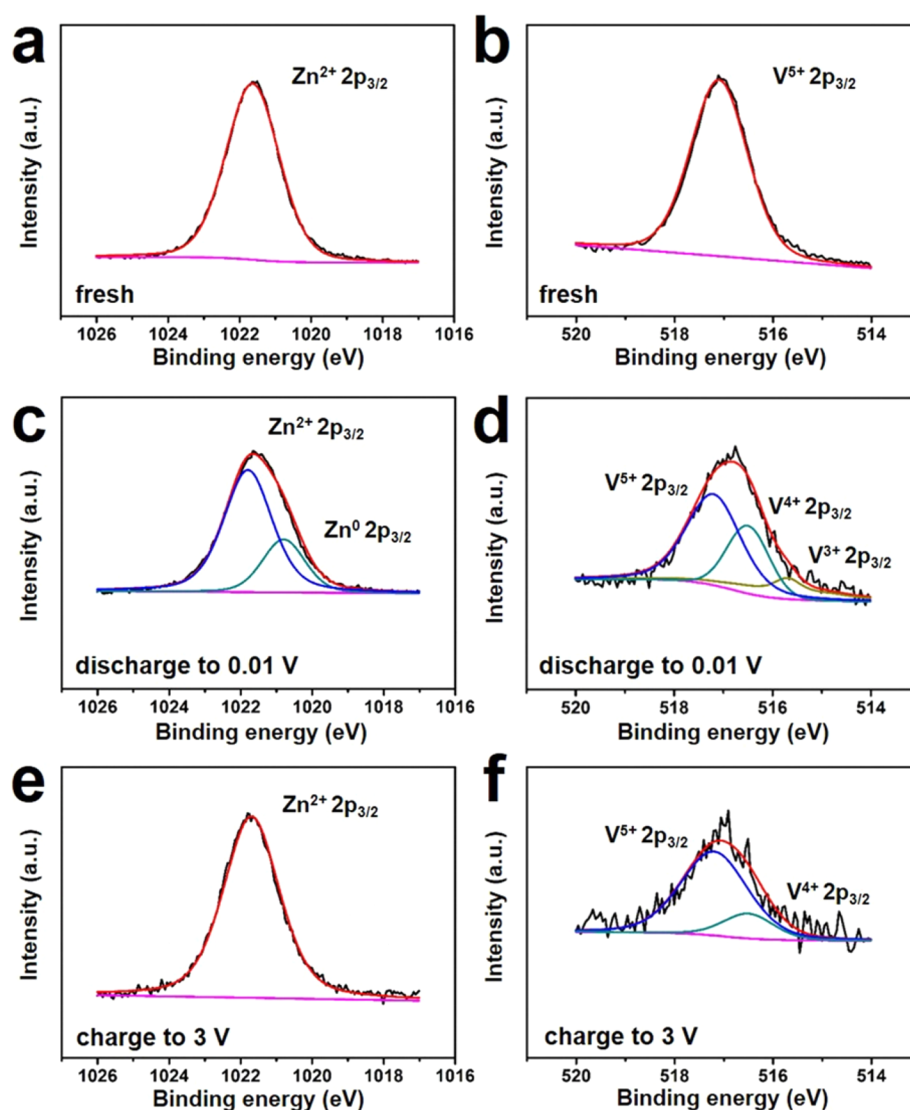
Figure 5. XPS of (a,b) fresh-prepared electrode, (c,d) reduced electrode obtained at 0.01 V, and (e,f) reoxidized electrode obtained at 3 V of zinc pyrovanadate nanoplates embedded in graphene networks at a current density of 100 mA g^{-1}, respectively.

attributed to the D band (K-point phonons of A$_{1g}$ symmetry) and G band (E$_{2g}$ phonons of the C sp^2 atoms) of the graphene, respectively.[55] Compared to GO, the G band shifts to low frequency, indicating a significant removal of oxygen containing groups on the GO surface during the high temperature hydrothermal process.[56] Furthermore, the ZVO-GN sample shows a lower I_D to I_G ratio ($I_D/I_G = 0.94$) when compared to the GO precursor ($I_D/I_G = 1.47$), indicating the electronic conjugation after reduction.[57]

To confirm the composition of the product, thermogravimetric analysis measurements were performed in a flowing air atmosphere. The TG curve of ZVO displays that the weight loss mainly proceeded in three steps, giving a total weight loss of ~11.19% up to 700 °C (black curve, Figure S3b). First, a little weight loss below 120 °C could be attributed to the loss of moisture in the sample. Second, ~ 7.70% weight loss below 240 °C may be due to the release of crystal water. Third, ~ 3.49% weight loss at 240−400 °C can be attributed to the decomposition of zinc pyrovanadate (the removal of coordinated water). It is calculated that the theoretical value of the water is 11.27% in Zn$_3$V$_2$O$_7$(OH)$_2$·2H$_2$O. Therefore, the phase

of as-synthesized products is suggested to be Zn$_3$V$_2$O$_7$(OH)$_2$· 2H$_2$O. The weight ratio of graphene in the ZVO-GN is ~3.48% (red curve, Figure S3b), which is consistent with carbon content (~3.63%) in the composite, according to carbon content analysis (Table S1). The N$_2$ adsorption/desorption measurement indicated that the as-prepared ZVO-GN has a Brunauer−Emmett−Teller (BET) surface area of ~9.95 m^2 g^{-1} (Figure S4b) larger than that of ZVO (~5.95 m^2 g^{-1}, Figure S4a).

The CV curves (Figure 4a) show a weak reduction peak observed at ~0.23 V of the first cycle, which may be attributed to the formation of a Li−Zn alloy.[22,58] The sharp peak at 0.45 V of the first cycle can be assigned to the formation of a solid electrolyte interphase (SEI) layer and the reduction of Zn^{2+} and V^{5+}, which is responsible for the irreversible capacity loss in the first cycle.[22,27,59] In the subsequent cycles, the main reduction peaks shift to 0.47 and 0.73 V, corresponding to the reduction of Zn and V, respectively. The broad oxidation peaks at 1.25 V in the three cycles may be attributed to the oxidation of V^{3+} to V^{5+} and Zn^0 to Zn^{2+}.[19,22] The areas of CV curves for ZVO (Figure S5a) are smaller than those of ZVO-GN, indicating that

the capacity of ZVO is lower than that of ZVO-GN. The specific capacity of the electrode is calculated based on the ZVO-GN nanocomposite. The galvanostatic discharge−charge voltage profiles for the 1st, 2nd, 50th, 100th, and 200th cycles of ZVO-GN and ZVO were collected at a current density of 200 mA g^{-1} (Figure 4b and Figure S5b). ZVO-GN presents a first cycle discharge capacity up to 1420 mA h g^{-1} with the Coulombic efficiency of ∼67%. ZVO-GN shows the capacity retention 98% from 2nd to 200th cycle, while ZVO shows a great decay of capacity after 200 cycles. ZVO-GN exhibits better rate performance than ZVO (Figure 4c). The average discharge capacities of 1134, 1008, 858, 732, and 629 mA h g^{-1} were obtained for ZVO-GN at current densities of 100, 200, 500, 1000, and 2000 mA g^{-1}, respectively. As for ZVO, its average reversible capacities are 991, 809, 628, 503, 375 mA h g^{-1} at the aforementioned current densities. When the current density is gradually reduced to 100 mA g^{-1} again, a capacity up to 1049 mA h g^{-1} (∼93% of the second cycle capacity) can be recovered for ZVO-GN. In contrast to ZVO-GN, a lower capacity of only 723 mA h g^{-1} (∼73% of the second cycle capacity) can be recovered for ZVO. Nyquist plots before and after cycling (Figure 4d) present a semicircle and a quasi-straight line, which are associated with the charge transfer resistance (R_{ct}) and the impedance of Li^{+} diffusion in solid materials (Warburg impedance, Z_w), respectively. Moreover, the values of R_{ct} for ZVO-GN are obviously lower than those for pristine ZVO, indicating a better electronic contact of the ZVO-GN electrode superior to the ZVO electrode. The values of R_{ct} decrease after discharging/charging for both electrodes, indicating a decrease in resistance after cycling.

Besides high capacity and good rate capability, ZVO-GN also shows excellent cycling performance (Figure 4e). Its first discharge and charge capacity is 1396 mA h g^{-1} and 902 mA h g^{-1}, respectively, corresponding to a Coulombic efficiency of ∼65%. After 400 cycles, the nanocomposite retains a high capacity of 854 mA h g^{-1} at a current density of 500 mA g^{-1} and maintains ∼95% of the second cycle discharge capacity. It is worth mentioning that the capacity of rGO is only ∼84 mA h g^{-1} after 100 cycles at a current density of 200 mA g^{-1} (Figure S6), indicating that rGO contributes little to the capacity of the nanocomposite. Cycling performances of ZVO-GN at different current densities (Figure S7 and Table S2) demonstrate the higher capacity and better cyclability than those of ZVO. To show the effects of crystal water on electrochemical performance, two control samples have been prepared. Both of their electrochemical performances are inferior to that of pristine ZVO (Figure S8). In addition, the results of another two control experiments indicate that the ZVO-GN composite synthesized via hydrothermal method shows better electrochemical performance than both physical mixtures of ZVO and rGO and bare ZVO nanoplates, and that the amount of conductive additives has no side effect on the cycling performance of ZVO-GN (Figures S9 and S10).

To elucidate the reason for the better cyclability of ZVO-GN than that of ZVO, SEM images of ZVO and ZVO-GN after cycling were carried out (Figure S11). After 50 cycles at a current density of 500 mA g^{-1}, ZVO nanoplates pulverize with some nanoparticles agglomerating around the nanoplates due to the volumetric change of the materials during lithiation and delithiation (Figure S11a,b). However, the morphology of ZVO-GN is well-preserved (Figure S11c,d) under the same condition, indicating better structural integrity of ZVO-GN than that of pristine ZVO during repeated Li^{+} insertion/

extraction. On the basis of the results above, the better rate capability and cycling performance of ZVO-GN is attributed to the hybrid architecture. On the one hand, conductive graphene networks offer efficient electron transport and provide mechanical flexibility for ZVO to accommodate volumetric variations and prevent the pulverization during cycling (Figure S11). On the other hand, compared with bare ZVO, the hybrid structure possesses higher contact area between electrode and electrolyte to reduce R_{ct} (Figure S4, Figure 4d), which results in better rate capability.

To further investigate the electrochemical reaction mechanism, ex-situ XPS spectra are employed to monitor the valence states change of Zn and V. In the XPS spectra of the fresh-prepared ZVO-GN electrode, the peak located at the binding energy of 1021.6 eV is attributed to Zn^{2+} 2p$_{3/2}$ and the peak for V 2p$_{3/2}$ (517.1 eV) can be indexed to V^{5+}, suggesting the Zn element and V element exist as Zn^{2+} and V^{5+}, respectively (Figure 5a,b). For the electrode discharged to 0.01 V in first cycle, the peak for Zn 2p$_{3/2}$ can be deconvoluted into two components, where a new small peak beside Zn^{2+} appears at the binding energy of 1021.4 eV, corresponding to the Zn^{0} state. Upon deep discharge, Zn can reversibly react with Li to form a Li−Zn alloy at potentials below 1.0 V and contribute to the anodic capacity.[60] Because of the valence state change of V, the peak becomes broadened. Further analysis indicates that the XPS peak has three components at 517.2, 516.5, and 515.7 eV, corresponding to V^{5+}, V^{4+}, and V^{3+}, respectively, implying the reduction of V^{5+} to V^{4+} and consecutive reduction of V^{4+} to V^{3+} in the discharge process (Figure 5c,d). When the electrode charged to 3 V, the Zn^{0} is oxidized to Zn^{2+} again during the subsequent delithiation process (Figure 5e). In the V 2p$_{3/2}$ spectrum, the vanadium is not fully recovered to V^{5+}, with the existence of V^{4+} (Figure 5f), which correspond to those reported transition metal vanadates.[19,22,27]

The results demonstrate that zinc pyrovanadate nanoplates embedded in graphene networks show better electrochemical performance compared to pristine zinc pyrovanadate nanoplates. The improved electrochemical performance can be ascribed to two factors: First, this nanocomposite possesses higher specific area than that of pristine zinc pyrovanadate nanoplates, indicating that the nanocomposite has a large electrode−electrolyte contact area and provides more active reaction sites to reduce the R_{ct}. Second, graphene offers 2D continuous networks to improve the electronic conductivity and increases structural integrity for good strain accommodation. The good electrochemical properties of the nanocomposite make it a promising anode material for LIBs.

■ CONCLUSIONS

In this work, zinc pyrovanadate nanoplates embedded in graphene networks were successfully synthesized via a facile one-pot hydrothermal method. This architecture utilizes the advantages of enhanced conductivity and structural-integrity for graphene and high specific capacity for zinc pyrovanadate nanoplates. The nanocomposite exhibits a superior cyclability from second to 400th cycle at a current density of 500 mA g^{-1} with a 95% of capacity retention. The design and construction of hybrid nanostructure in this work is a facile and effective method to fabricate stable and high-performance materials for LIBs.

ASSOCIATED CONTENT

Ⓢ Supporting Information

The Supporting Information is available free of charge on the ACS Publications website at DOI: 10.1021/acs.iecr.5b04811.

Crystal structure of $Zn_3V_2O_7(OH)_2 \cdot 2H_2O$ phase; XRD pattern of ZVO-GN; Raman spectra of ZVO-GN and GO; TG curves of ZVO and ZVO-GN; N_2 adsorption/desorption isotherms of ZVO and ZVO-GN; carbon content analysis of ZVO-GN; CV curves and discharge/charge profiles of ZVO; cycling performance of pure GO; comparison of cycling performance between ZVO and ZVO-GN at different current densities; comparison of electrochemical performance between this work and other previous works (PDF)

AUTHOR INFORMATION

Corresponding Authors

*E-mail: hch5927@gmail.com.
*E-mail: mlq518@whut.edu.cn.

Author Contributions

#Y.Y. and C.N. contributed equally to this work.

Notes

The authors declare no competing financial interest.

ACKNOWLEDGMENTS

REFERENCES

(1) Simon, P.; Gogotsi, Y.; Dunn, B. Where do batteries end and supercapacitors begin? *Science* **2014**, *343*, 1210.

(2) Yoshino, A. The Birth of the Lithium-Ion Battery. *Angew. Chem., Int. Ed.* **2012**, *51*, 5798.

(3) Armand, M.; Tarascon, J. M. Building better batteries. *Nature* **2008**, *451*, 652.

(4) Van Noorden, R. The rechargeable revolution: A better battery. *Nature* **2014**, *507*, 26.

(5) Dunn, B.; Kamath, H.; Tarascon, J.-M. Electrical energy storage for the grid: a battery of choices. *Science* **2011**, *334*, 928.

(6) Wu, H.; Chan, G.; Choi, J. W.; Yao, Y.; McDowell, M. T.; Lee, S. W.; Jackson, A.; Yang, Y.; Hu, L.; Cui, Y. Stable cycling of double-walled silicon nanotube battery anodes through solid-electrolyte interphase control. *Nat. Nanotechnol.* **2012**, *7*, 310.

(7) Mai, L.; Tian, X.; Xu, X.; Chang, L.; Xu, L. Nanowire electrodes for electrochemical energy storage devices. *Chem. Rev.* **2014**, *114*, 11828.

(8) Sasaki, T.; Ukyo, Y.; Novák, P. Memory effect in a lithium-ion battery. *Nat. Mater.* **2013**, *12*, 569.

(9) Yao, Y.; McDowell, M. T.; Ryu, I.; Wu, H.; Liu, N.; Hu, L.; Nix, W. D.; Cui, Y. Interconnected silicon hollow nanospheres for lithium-ion battery anodes with long cycle life. *Nano Lett.* **2011**, *11*, 2949.

(10) Bruce, P. G.; Scrosati, B.; Tarascon, J. M. Nanomaterials for rechargeable lithium batteries. *Angew. Chem., Int. Ed.* **2008**, *47*, 2930.

(11) Wang, Z.; Zhou, L.; Lou, X. W. Metal Oxide Hollow Nanostructures for Lithium-ion Batteries. *Adv. Mater.* **2012**, *24*, 1903.

(12) Yuan, C.; Wu, H. B.; Xie, Y.; Lou, X. W. D. Mixed Transition-Metal Oxides: Design, Synthesis, and Energy-Related Applications. *Angew. Chem., Int. Ed.* **2014**, *53*, 1488.

(13) Wu, F.; Bai, J.; Feng, J.; Xiong, S. Porous mixed metal oxides: design, formation mechanism, and application in lithium-ion batteries. *Nanoscale* **2015**, *7*, 17211.

(14) Ni, J.; Zhao, Y.; Li, L.; Mai, L. Ultrathin MoO_2 nanosheets for superior lithium storage. *Nano Energy* **2015**, *11*, 129.

(15) Zhang, K.; Han, X.; Hu, Z.; Zhang, X.; Tao, Z.; Chen, J. Nanostructured Mn-based oxides for electrochemical energy storage and conversion. *Chem. Soc. Rev.* **2015**, *44*, 699.

(16) Jiang, J.; Li, Y.; Liu, J.; Huang, X.; Yuan, C.; Lou, X. W. D. Recent advances in metal oxide-based electrode architecture design for electrochemical energy storage. *Adv. Mater.* **2012**, *24*, 5166.

(17) Wu, H. B.; Chen, J. S.; Hng, H. H.; Lou, X. W. D. Nanostructured metal oxide-based materials as advanced anodes for lithium-ion batteries. *Nanoscale* **2012**, *4*, 2526.

(18) Ma, H.; Zhang, S.; Ji, W.; Tao, Z.; Chen, J. α-CuV_2O_6 nanowires: Hydrothermal synthesis and primary lithium battery application. *J. Am. Chem. Soc.* **2008**, *130*, 5361.

(19) Wu, F.; Yu, C.; Liu, W.; Wang, T.; Feng, J.; Xiong, S. Large-scale synthesis of $Co_2V_2O_7$ hexagonal microplatelets under ambient conditions for highly reversible lithium storage. *J. Mater. Chem. A* **2015**, *3*, 16728.

(20) Xiao, L.; Zhao, Y.; Yin, J.; Zhang, L. Clewlike ZnV_2O_4 hollow spheres: Nonaqueous sol-gel synthesis, formation mechanism, and lithium storage properties. *Chem. - Eur. J.* **2009**, *15*, 9442.

(21) Sun, Y.; Li, C.; Wang, L.; Wang, Y.; Ma, X.; Ma, P.; Song, M. Ultralong monoclinic ZnV_2O_6 nanowires: their shape-controlled synthesis, new growth mechanism, and highly reversible lithium storage in lithium-ion batteries. *RSC Adv.* **2012**, *2*, 8110.

(22) Gan, L.-H.; Deng, D.; Zhang, Y.; Li, G.; Wang, X.; Jiang, L.; Wang, C.-R. $Zn_3V_2O_8$ hexagon nanosheets: a high-performance anode material for lithium-ion batteries. *J. Mater. Chem. A* **2014**, *2*, 2461.

(23) Zhang, S.; Ci, L.; Liu, H. Synthesis, characterization, and electrochemical properties of $Cu_3V_2O_7 (OH)_2 \cdot 2H_2O$ nanostructures. *J. Phys. Chem. C* **2009**, *113*, 8624.

(24) Wu, F.; Xiong, S.; Qian, Y.; Yu, S. H. Hydrothermal Synthesis of Unique Hollow Hexagonal Prismatic Pencils of $Co_3V_2O_8 \cdot nH_2O$: A New Anode Material for Lithium-Ion Batteries. *Angew. Chem., Int. Ed.* **2015**, *54*, 10787.

(25) Zeng, L.; Xiao, F.; Wang, J.; Gao, S.; Ding, X.; Wei, M. ZnV_2O_4-CMK nanocomposite as an anode material for rechargeable lithium-ion batteries. *J. Mater. Chem.* **2012**, *22*, 14284.

(26) Hu, W.; Zhang, X.-B.; Cheng, Y.-L.; Wu, Y.-M.; Wang, L.-M. Low-cost and facile one-pot synthesis of pure single-crystalline ε-$Cu_{0.95}V_2O_5$ nanoribbons: high capacity cathode material for rechargeable Li-ion batteries. *Chem. Commun.* **2011**, *47*, 5250.

(27) Yang, G.; Cui, H.; Yang, G.; Wang, C. Self-assembly of $Co_3V_2O_8$ multilayered nanosheets: controllable synthesis, excellent Li-storage properties, and investigation of electrochemical mechanism. *ACS Nano* **2014**, *8*, 4474.

(28) Sim, D. H.; Rui, X.; Chen, J.; Tan, H.; Lim, T. M.; Yazami, R.; Hng, H. H.; Yan, Q. Direct growth of $FeVO_4$ nanosheet arrays on stainless steel foil as high-performance binder-free Li ion battery anode. *RSC Adv.* **2012**, *2*, 3630.

(29) Zhao, K.; Liu, F.; Niu, C.; Xu, W.; Dong, Y.; Zhang, L.; Xie, S.; Yan, M.; Wei, Q.; Zhao, D.et al. Graphene Oxide Wrapped Amorphous Copper Vanadium Oxide with Enhanced Capacitive Behavior for High-Rate and Long-Life Lithium-Ion Battery Anodes. *Adv. Sci.* **2015**, *2*. doi: 10.1002/advs.201500154.

(30) Hu, Y.-Y.; Liu, Z.; Nam, K.-W.; Borkiewicz, O. J.; Cheng, J.; Hua, X.; Dunstan, M. T.; Yu, X.; Wiaderek, K. M.; Du, L.-S.; et al. Origin of additional capacities in metal oxide lithium-ion battery electrodes. *Nat. Mater.* **2013**, *12*, 1130.

(31) Nam, K. W.; Kim, S.; Lee, S.; Salama, M.; Shterenberg, I.; Gofer, Y.; Kim, J.-S.; Yang, E.; Park, C. S.; Kim, J.-S.; et al. The High Performance of Crystal Water Containing Manganese Birnessite Cathodes for Magnesium Batteries. *Nano Lett.* **2015**, *15*, 4071.

(32) Poizot, P.; Baudrin, E.; Laruelle, S.; Dupont, L.; Touboul, M.; Tarascon, J.-M. Low temperature synthesis and electrochemical performance of crystallized FeVO$_4$·1.1H$_2$O. *Solid State Ionics* **2000**, *138*, 31.

(33) Zheng, C.; Zeng, L.; Wang, M.; Zheng, H.; Wei, M. Synthesis of hierarchical ZnV$_2$O$_4$ microspheres and its electrochemical properties. *CrystEngComm* **2014**, *16*, 10309.

(34) Zhang, S.; Lei, N.; Ma, W.; Zhang, Z.; Sun, Z.; Wang, Y. Fabrication of ultralong Zn$_3$V$_2$O$_7$(OH)$_2$·2H$_2$O nanobelts and its application in lithium-ion batteries. *Mater. Lett.* **2014**, *129*, 91.

(35) Zhang, S. Y.; Xiao, X.; Lu, M.; Li, Z. Q. Zn$_3$V$_2$O$_7$ (OH)$_2$· 2H$_2$O and Zn$_3$(VO$_4$)$_2$ 3D microspheres as anode materials for lithium-ion batteries. *J. Mater. Sci.* **2013**, *48*, 3679.

(36) Cheng, F.; Chen, J. Transition metal vanadium oxides and vanadate materials for lithium batteries. *J. Mater. Chem.* **2011**, *21*, 9841.

(37) Sun, Y.; Wu, Q.; Shi, G. Graphene based new energy materials. *Energy Environ. Sci.* **2011**, *4*, 1113.

(38) Zhang, L. L.; Zhou, R.; Zhao, X. Graphene-based materials as supercapacitor electrodes. *J. Mater. Chem.* **2010**, *20*, 5983.

(39) Pumera, M. Graphene-based nanomaterials and their electro-chemistry. *Chem. Soc. Rev.* **2010**, *39*, 4146.

(40) Chen, C.; Wen, Y.; Hu, X.; Ji, X.; Yan, M.; Mai, L.; Hu, P.; Shan, B.; Huang, Y. Na$^+$ intercalation pseudocapacitance in graphene-coupled titanium oxide enabling ultra-fast sodium storage and long-term cycling. *Nat. Commun.* **2015**, *6*, 6929.

(41) Gao, G.; Wu, H. B.; Dong, B.; Ding, S.; Lou, X. W. D. Growth of Ultrathin ZnCo$_2$O$_4$ Nanosheets on Reduced Graphene Oxide with Enhanced Lithium Storage Properties. *Adv. Sci.* **2015**, *2*, doi: 10.1002/advs.201400014.

(42) Qu, B.; Ma, C.; Ji, G.; Xu, C.; Xu, J.; Meng, Y. S.; Wang, T.; Lee, J. Y. Layered SnS$_2$-Reduced Graphene Oxide Composite-A High-Capacity, High-Rate, and Long-Cycle Life Sodium-Ion Battery Anode Material. *Adv. Mater.* **2014**, *26*, 3854.

(43) Qin, J.; He, C.; Zhao, N.; Wang, Z.; Shi, C.; Liu, E.-Z.; Li, J. Graphene Networks Anchored with Sn@Graphene as Lithium Ion Battery Anode. *ACS Nano* **2014**, *8*, 1728.

(44) An, Q.; Lv, F.; Liu, Q.; Han, C.; Zhao, K.; Sheng, J.; Wei, Q.; Yan, M.; Mai, L. Amorphous vanadium oxide matrixes supporting hierarchical porous Fe$_3$O$_4$/graphene nanowires as a high-rate lithium storage anode. *Nano Lett.* **2014**, *14*, 6250.

(45) Jian, Z.; Zheng, M.; Liang, Y.; Zhang, X.; Gheytani, S.; Lan, Y.; Shi, Y.; Yao, Y. Li$_3$VO$_4$ anchored graphene nanosheets for long-life and high-rate lithium-ion batteries. *Chem. Commun.* **2015**, *51*, 229.

(46) Wu, C.; Maier, J.; Yu, Y. Sn-Based Nanoparticles Encapsulated in a Porous 3D Graphene Network: Advanced Anodes for High-Rate and Long Life Li-Ion Batteries. *Adv. Funct. Mater.* **2015**, *25*, 3488.

(47) Rui, X.; Sun, W.; Wu, C.; Yu, Y.; Yan, Q. An Advanced Sodium-Ion Battery Composed of Carbon Coated Na$_3$V$_2$(PO$_4$)$_3$ in a Porous Graphene Network. *Adv. Mater.* **2015**, *27*, 6670.

(48) An, Q.; Li, Y.; Yoo, H. D.; Chen, S.; Ru, Q.; Mai, L.; Yao, Y. Graphene decorated vanadium oxide nanowire aerogel for long-cycle-life magnesium battery cathodes. *Nano Energy* **2015**, *18*, 265.

(49) Song, H.; Li, N.; Cui, H.; Wang, C. Enhanced capability and cyclability of SnO$_2$-graphene oxide hybrid anode by firmly anchored SnO$_2$ quantum dots. *J. Mater. Chem. A* **2013**, *1*, 7558.

(50) Gao, G.; Wu, H. B.; Lou, X. W. D. Citrate-Assisted Growth of NiCo$_2$O$_4$ Nanosheets on Reduced Graphene Oxide for Highly Reversible Lithium Storage. *Adv. Energy Mater.* **2014**, *4*, doi: 10.1002/aenm.201400422.

(51) Marcano, D. C.; Kosynkin, D. V.; Berlin, J. M.; Sinitskii, A.; Sun, Z.; Slesarev, A.; Alemany, L. B.; Lu, W.; Tour, J. M. Improved synthesis of graphene oxide. *ACS Nano* **2010**, *4*, 4806.

(52) Livage, J. Vanadium pentoxide gels. *Chem. Mater.* **1991**, *3*, 578.

(53) Zavalij, P. Y.; Zhang, F.; Whittingham, M. S. A new zinc pyrovanadate, Zn$_3$(OH)$_2$V$_2$O$_7$·2H$_2$O, from X-ray powder data. *Acta Crystallogr., Sect. C: Cryst. Struct. Commun.* **1997**, *53*, 1738.

(54) Zavalij, P. Y.; Zhang, F.; Whittingham, M. S. The zinc-vanadium-oxygen-water system: hydrothermal synthesis and character-ization. *Solid State Sci.* **2002**, *4*, 591.

(55) Wu, C.; Kopold, P.; Ding, Y.-L.; van Aken, P. A.; Maier, J.; Yu, Y. Synthesizing Porous NaTi$_2$(PO$_4$)$_3$ Nanoparticles Embedded in 3D Graphene Networks for High-Rate and Long Cycle-Life Sodium Electrodes. *ACS Nano* **2015**, *9*, 6610.

(56) Kudin, K. N.; Ozbas, B.; Schniepp, H. C.; Prud'Homme, R. K.; Aksay, I. A.; Car, R. Raman spectra of graphite oxide and functionalized graphene sheets. *Nano Lett.* **2008**, *8*, 36.

(57) Kosynkin, D. V.; Higginbotham, A. L.; Sinitskii, A.; Lomeda, J. R.; Dimiev, A.; Price, B. K.; Tour, J. M. Longitudinal unzipping of carbon nanotubes to form graphene nanoribbons. *Nature* **2009**, *458*, 872.

(58) Shen, L.; Wang, C. ZnO/C microboxes derived from coordination polymer particles for superior lithium ion battery anodes. *RSC Adv.* **2015**, *5*, 88989.

(59) Bai, J.; Li, X.; Liu, G.; Qian, Y.; Xiong, S. Unusual Formation of ZnCo$_2$O$_4$ 3D Hierarchical Twin Microspheres as a High-Rate and Ultralong-Life Lithium-Ion Battery Anode Material. *Adv. Funct. Mater.* **2014**, *24*, 3012.

(60) Li, H.; Huang, X.; Chen, L. Anodes based on oxide materials for lithium rechargeable batteries. *Solid State Ionics* **1999**, *123*, 189.